Computers & Fluids 41 (2011) 27–40

Contents lists available at ScienceDirect

Computers & Fluids

journal homepage: www.elsevier.com/locate/compfluid

Computational simulation of model and full scale Class 8 trucks with drag reduction devices

Daniel G. Hyams *, Kidambi Sreenivas, Ramesh Pankajakshan, D. Stephen Nichols, W. Roger Briley, David L. Whitfield

SimCenter: National Center for Computational Engineering, University of Tennessee at Chattanooga, TN 37403, USA

ARTICLE INFO

Article history:
Available online 21 September 2010

Keywords:
Parallel implicit algorithm
Heavy trucks
Unstructured grid
Navier–Stokes
Preconditioning
Drag reduction

ABSTRACT

Numerical solutions of the unsteady Reynolds-averaged Navier–Stokes equations using a parallel implicit flow solver are given to investigate unsteady aerodynamic flows affecting the fuel economy of Class 8 trucks. Both compressible and incompressible forms of the equations are solved using a finite-volume discretization for unstructured grids and using Riemann-based interfacial fluxes and characteristic-variable numerical boundary conditions. A preconditioned primitive-variable formulation is used for compressible solutions, and the incompressible solutions employ artificial compressibility. Detached eddy simulation (DES) versions of the one-equation Menter SAS and the two-equation $k-\epsilon/k-\omega$ hybrid turbulence models are used. A fully nonlinear implicit backward-time approximation is solved using a parallel Newton-iterative algorithm with numerically computed flux Jacobians. Unsteady three-dimensional aerodynamic simulations with grids of 18–20 million points and 50,000 time steps are given for the Generic Conventional Model (GCM), a 1:8 scale tractor–trailer model that was tested in the NASA Ames 7 × 10 tunnel. Computed pressure coefficients and drag force are in good agreement with measurements for a zero-incidence case. Similar computations for a case with 10° yaw gave reasonable agreement for drag force, while the pressure distributions suggested the need for tighter grid resolution or possibly improved turbulence models. Unsteady incompressible flow simulations were performed for a modified full scale version of the GCM geometry to evaluate drag reduction devices. All of these simulations were performed with a moving ground plane and rotating rear wheels. A simulation with trailer base flaps is compared with drag reduction data from wind tunnels and track and road tests. A front spoiler and three mud-flap designs with modest drag reduction potential are also evaluated.

1. Introduction

Recent advances in unstructured grids and solution algorithms, coupled with current parallel computing hardware and software, have enabled unsteady three-dimensional flow simulations for complex geometric configurations at much higher resolution and fidelity than was feasible in the past. As a consequence, it has become possible to perform large-scale simulations that contribute to our understanding of many important practical flow problems. In the present study, simulations with grids of 18–20 million points and 50,000 time steps were performed to investigate unsteady aerodynamic flows affecting the fuel economy of Class 8 trucks.

In 1997, fuel consumption among Class 8 trucks was 18 billion gallons [1]. At typical highway speeds (70 mph), 65% of the overall output of the engine is used for overcoming aerodynamic drag [2]. Consequently, even small reductions in aerodynamic drag are expected to result in substantial fuel savings. Given the large number of tractor/trailers in use in the United States, this could translate into a significant reduction in domestic fuel consumption as well as a reduction in vehicle emissions.

While a large number of effective drag reduction devices have been developed and are commercially available [1], adoption in the trucking industry has been relatively insignificant due to infrastructure, legislative, maintenance, staffing, and aftermarket barriers which have rendered them cost ineffective to the majority of trucking companies. A good example of such technology is the base flap, which has seen slow adoption in spite of drag reductions in excess of 10%. While there clearly is the potential for substantial drag reduction in the base region of the trailer, any changes to this area of the truck have to be made in light of severe restrictions imposed by existing infrastructure and operational norms. The underbody of the truck offers an area with less potential but with the type of restrictions which are more amenable to engineering solutions. Moreover, drag reduction devices which target consumables like mud flaps are more likely to be tried and adopted, since they

* Corresponding author.
E-mail address: Daniel-Hyams@utc.edu (D.G. Hyams).

0045-7930/$ - see front matter © 2010 Elsevier Ltd. All rights reserved.
doi:10.1016/j.compfluid.2010.09.015

must often be changed due to normal wear. The underbody is, however, by no means a blank slate on which the aerodynamicist may impose his/her will; there are practical restrictions in terms of ground clearance and ease of access for maintenance and inspection which have proven to prevent the adoption of extant devices such as side skirts. There are also less obvious issues such as the effect of any drag devices on brake cooling flows, as well as splash and spray.

The main contributors to the aerodynamic drag are the gap between tractor and trailer, the vehicle underbody, and the base flow region of the trailer [3]. Significant flow structures exist in these regions and several experimental studies have been carried out to characterize them. One of the experimental studies used a 1:8 scale Ground Transportation System (GTS) model that consisted of simplified tractor–trailer geometry with a cab-over-engine design and no tractor–trailer gap. This geometry was tested both at the Texas A& M University Low Speed Wind Tunnel [4] as well as the NASA Ames $7' \times 10'$ tunnel [5], and extensive data was collected for validation of computational simulations. Modifications to the GTS geometry to include a tractor–trailer gap were incorporated in tests carried out at USC [6] and the influence of the gap on the overall flowfield assessed. Detailed experimental studies were also carried out on a realistic tractor–trailer combination, the Generic Conventional Model (GCM), in the NASA Ames $7' \times 10'$ as well as the $12'$ wind tunnel [7].

Computational studies aimed at evaluating the capabilities of current flow solvers for the prediction of heavy vehicle aerodynamics have been carried out by a number of researchers [8–12]. Salari et al. [8] used the data from the GTS experiments and showed that with an appropriate choice of turbulence model, the overall drag coefficient could be predicted with reasonable accuracy. However, one of their key findings was that the details of the flow field, especially in the base flow region, were not being captured accurately. Pointer [9] used a commercial CFD flow solver to study the GCM model in the $7' \times 10'$ tunnel, and the results indicated that the overall drag coefficient could be predicted with reasonable accuracy; however, no detailed flow field comparisons were presented. Maddox et al. [10] used another commercial CFD solver to simulate the flow around the GTS model. They employed a detached eddy simulation (DES) approach and showed that an improvement in the predicted pressure (especially toward the base of the model) can be achieved. RANS simulations using the one-equation Spalart–Allmaras model and the two-equation Menter $k-\omega$ model were reported by Roy et al. [11] LES simulations of a truncated GTS model were carried out by Ortega et al. [12].

The present research effort focuses on *Tenasi*, a family of structured and unstructured flow solvers that has been developed at the University of Tennessee SimCenter at Chattanooga. The unstructured flow solver is used to simulate the flowfield around the GCM model inside the NASA $7' \times 10'$ tunnel at 0 and 10° yaw, as well as simulate the effect of various drag reduction devices on a full scale Class 8 truck.

2. Governing equations

The *Tenasi* code, as utilized in this work, is capable of simulating both high speed and low speed flow effectively via an unsteady Reynolds-averaged Navier–Stokes (unRANS) approach. For flows that consist of both high and low speed regions, an arbitrary Mach number variation of the flow solver, as presented in Sreenivas et al. [13], is utilized; this formulation solves for the primitive variables ρ, u, v, w, and P. For flows in which compressibility effects can be neglected, an incompressible variation of the solver, similar to that given by Hyams et al. [14,15], may be utilized, which solves for the variables P, u, v, and w. Both formulations follow the basic form of the Navier–Stokes equations applicable to general unstructured grids with mixed element shapes. Eq. (1) is written as an integral conservation equation for a volume Ω enclosed by a surface $\partial\Omega$:

$$\frac{\partial}{\partial t}\int_{\Omega}\mathbf{Q}(q)d\mathscr{V} + \oint_{\partial\Omega}\vec{\boldsymbol{F}}\cdot\hat{\vec{n}}d\mathscr{S} = \frac{1}{Re}\oint_{\partial\Omega}\vec{\boldsymbol{G}}\cdot\hat{\vec{n}}d\mathscr{S} + \int_{\Omega}\boldsymbol{S}d\mathscr{V} \tag{1}$$

with appropriate definitions for the solution vector $\boldsymbol{Q}$, flux vector $\boldsymbol{F}$, viscous flux vector $\boldsymbol{G}$, and source term $\boldsymbol{S}$. Definitions for these quantities are to be given in the following subsections. $d\mathscr{V}$ denotes a differential volume of Ω, and $d\mathscr{S}$ denotes a differential surface area of the enclosing volumetric surface $\partial\Omega$, whose outward-facing normal unit vector is $\hat{\vec{n}}$. For the cases presented in this work, the source term $\boldsymbol{S}$ is the zero vector.

All equations are nondimensionalized with respect to a reference velocity U_r, density ρ_r, characteristic length scale L, reference enthalpy h_r (equal to C_pT_r for a perfect gas with constant specific heat) and a reference molecular viscosity μ_r. Thus, $Re = \rho_r U_r L/\mu_r$. The nondimensional pressure is defined as $P = (P^* - P_g)/(\rho_r U_r^2)$, where P^* is the local static pressure, and P_g is a gauge pressure selected by the practitioner. For the incompressible formulation, ρ_r is obviously not needed; also, since no energy equation appears in the incompressible case, h_r is not needed. Further detail of the nondimensionalization is given in [16]. In this work, reference values were chosen to match freestream/wind-tunnel conditions.

2.1. Incompressible formulation

The incompressible solver utilizes the artificial compressibility approach of Chorin [17]. In this case, the solution vector and flux vector are defined as

$$\boldsymbol{q} = \mathbf{Q}(q) = \begin{bmatrix} P \\ u \\ v \\ w \end{bmatrix} \tag{2}$$

$$\vec{\boldsymbol{F}} = \begin{bmatrix} \beta u \\ u(u-V_x)+P \\ v(u-V_x) \\ w(u-V_x) \end{bmatrix}\hat{i} + \begin{bmatrix} \beta v \\ u(v-V_y) \\ v(v-V_y)+P \\ w(v-V_y) \end{bmatrix}\hat{j} + \begin{bmatrix} \beta w \\ u(w-V_z) \\ v(w-V_z) \\ w(w-V_z)+P \end{bmatrix}\hat{k} \tag{3}$$

$$\vec{\boldsymbol{G}} = \begin{bmatrix} 0 \\ \tau_{xx} \\ \tau_{yx} \\ \tau_{zx} \end{bmatrix}\hat{i} + \begin{bmatrix} 0 \\ \tau_{xy} \\ \tau_{yy} \\ \tau_{zy} \end{bmatrix}\hat{j} + \begin{bmatrix} 0 \\ \tau_{xz} \\ \tau_{yz} \\ \tau_{zz} \end{bmatrix}\hat{k} \tag{4}$$

where the shear stresses are given as

$$\tau_{xx} = 2(1+\mu_t)u_x \tag{5}$$
$$\tau_{yy} = 2(1+\mu_t)v_y \tag{6}$$
$$\tau_{zz} = 2(1+\mu_t)w_z \tag{7}$$
$$\tau_{xy} = \tau_{yx} = (1+\mu_t)(u_y+v_x) \tag{8}$$
$$\tau_{xz} = \tau_{zx} = (1+\mu_t)(u_z+w_x) \tag{9}$$
$$\tau_{yz} = \tau_{zy} = (1+\mu_t)(v_z+w_y) \tag{10}$$

and the velocity of the control volume face is given by the quantities V_x, V_y, and V_z. The Chorin artificial compressibility parameter β is typically set to a constant of 5.0. The eddy viscosity μ_t is determined by the solution of the turbulence model utilized.

2.2. Arbitrary mach number formulation

The solution vectors and flux vectors for the compressible Navier–Stokes equations are given below.

$$\mathbf{Q}(q) = \begin{bmatrix} \rho \\ \rho u \\ \rho v \\ \rho w \\ \rho e_t \end{bmatrix} \tag{11}$$

$$\boldsymbol{q} = \begin{bmatrix} \rho \\ u \\ v \\ w \\ P \end{bmatrix} \tag{12}$$

$$\vec{\boldsymbol{F}} = \begin{bmatrix} \rho(u - V_x) \\ \rho u(u - V_x) + P \\ \rho v(u - V_x) \\ \rho w(u - V_x) \\ \rho h_t(u - V_x) + V_x P \end{bmatrix} \hat{i} + \begin{bmatrix} \rho(v - V_y) \\ \rho u(v - V_y) \\ \rho v(v - V_y) + P \\ \rho w(v - V_y) \\ \rho h_t(v - V_y) + V_y P \end{bmatrix} \hat{j} + \begin{bmatrix} \rho(w - V_z) \\ \rho u(w - V_z) \\ \rho v(w - V_z) \\ \rho w(w - V_z) + P \\ \rho h_t(w - V_z) + V_z P \end{bmatrix} \hat{k} \tag{13}$$

$$\vec{\boldsymbol{G}} = \begin{bmatrix} 0 \\ \tau_{xx} \\ \tau_{yx} \\ \tau_{zx} \\ u\tau_{xx} + v\tau_{xy} + w\tau_{xz} - q_x \end{bmatrix} \hat{i} + \begin{bmatrix} 0 \\ \tau_{xy} \\ \tau_{yy} \\ \tau_{zy} \\ u\tau_{yx} + v\tau_{yy} + w\tau_{yz} - q_y \end{bmatrix} \hat{j} + \begin{bmatrix} 0 \\ \tau_{xz} \\ \tau_{yz} \\ \tau_{zz} \\ u\tau_{zx} + v\tau_{zy} + w\tau_{zz} - q_z \end{bmatrix} \hat{k} \tag{14}$$

where the shear stresses are given as

$$\tau_{xx} = (\mu + \mu_t)\left(2u_x - \frac{2}{3}\mathscr{D}\right) \tag{15}$$

$$\tau_{yy} = (\mu + \mu_t)\left(2v_y - \frac{2}{3}\mathscr{D}\right) \tag{16}$$

$$\tau_{zz} = (\mu + \mu_t)\left(2w_z - \frac{2}{3}\mathscr{D}\right) \tag{17}$$

$$\tau_{xy} = \tau_{yx} = (\mu + \mu_t)(u_y + v_x) \tag{18}$$

$$\tau_{xz} = \tau_{zx} = (\mu + \mu_t)(u_z + w_x) \tag{19}$$

$$\tau_{yz} = \tau_{zy} = (\mu + \mu_t)(v_z + w_y) \tag{20}$$

$$\vec{q} = -\frac{\frac{\mu}{Pr} + \frac{\mu_t}{Pr_t}}{(\gamma - 1)} \nabla T \tag{21}$$

$$\mathscr{D} = u_x + v_y + w_z \tag{22}$$

where Pr and Pr_t are the fluid Prandtl number and turbulent Prandtl number, respectively, and γ is the ratio of specific heats.

3. Numerical approach

The baseline flow solver in Tenasi employs a finite volume, implicit scheme with high resolution fluxes based on Roe averaging and a Newton subiteration procedure for time accuracy. The linear system at each Newton subiteration is solved using a Symmetric Gauss–Seidel algorithm. Some of the features of the unstructured solver are highlighted below.

3.1. Finite-volume discretization

The spatial discretization for a node-centered finite volume scheme is constructed from the median dual of a three-dimensional mixed-element unstructured grid. A control volume in this context implies a three-dimensional manifold from this median dual. The overall solution domain Ω is thereby divided into I non-overlapping control volumes Ω_i, $i = 1,2,\ldots,I$, each associated with a nodal point i. Each control volume Ω_i has a volume $\mathscr{V}_i = \int_{\Omega_i} d\mathscr{V}$. At each node, $\boldsymbol{q}_i$ denotes an volume averaged value defined by $\boldsymbol{q}_i = \left(\int_{\Omega_i} \boldsymbol{q} d\mathscr{V}\right)/\mathscr{V}_i$. Each point i is surrounding by a set $\mathscr{N}(i)$ of neighboring points denoted j, such that $j \in \mathscr{N}(i)$. Each control volume i is enclosed by a set of cell interfaces $\partial\Omega_{ij}$.

The surface flux integral in Eq. (1) is approximated by midpoint integration of the fluxes over each of the $\partial\Omega_{ij}$ interfaces that enclose the control volume. A simple and efficient technique for the midpoint integration is to evaluate the fluxes at the midpoint of the line connecting $\{ij\}$ and to represent the manifold surface interface $\partial\Omega_{ij}$ by a single resultant area vector, obtained by summing the area vectors resulting from the median dual discretization of the control volume. The area magnitude of this $\{ij\}$ cell interface is denoted $\delta\mathscr{S}_{ij}$, and its unit normal vector is denoted $\hat{\vec{\boldsymbol{n}}}_{ij}$. The surface flux integral is written as

$$\oint_{\partial\Omega_i} \vec{\boldsymbol{F}} \cdot \hat{\vec{n}} d\mathscr{S} \approx \sum_{j \in \mathscr{N}(i)} \boldsymbol{H}_{ij} \delta\mathscr{S}_{ij} \tag{23}$$

The numerical flux $\boldsymbol{H}_{ij}$ is given by

$$\boldsymbol{H}_{ij}(\boldsymbol{q}_L, \boldsymbol{q}_R) = \frac{1}{2}\left[(\boldsymbol{F}_L + \boldsymbol{F}_R) - \widetilde{\boldsymbol{M}}\widetilde{\boldsymbol{\Gamma}}_q^{-1}|\widetilde{\boldsymbol{\Gamma}}_q\tilde{\boldsymbol{a}}|(\boldsymbol{q}_R - \boldsymbol{q}_L)\right] \tag{24}$$

where $(\sim)$ indicates quantities evaluated with averaged state variables, $\boldsymbol{M} = \partial\boldsymbol{Q}/\partial\boldsymbol{q}$ is the transformation matrix from conservative to primitive variables, $\boldsymbol{\Gamma}_q = diag(1,1,1,1,\beta)$ is the preconditioning matrix, and $\boldsymbol{a} = \boldsymbol{M}^{-1}(\partial\boldsymbol{F}/\partial\boldsymbol{Q})\boldsymbol{M}$ is the system matrix for the primitive-variable form. The global preconditioning parameter β is defined as the square of the reference Mach number $M_r^2 = U_r^2/c_r^2$ for $M_r < 1$, and unity for $M_r > 1$. The primitive-variable flux is not sensitive to the type of averaging used for the state variables; an algebraic average $\bar{\boldsymbol{q}}$ is used unless otherwise noted. Further details of the development of this flux function in the context of the arbitrary Mach number algorithm can be found in [16,13]. For incompressible simulations, it should be noted that no preconditioning matrix is utilized, and $\boldsymbol{Q} = \boldsymbol{q}$. Therefore, $\boldsymbol{M} = \boldsymbol{I}$ and $\boldsymbol{\Gamma}_q = \boldsymbol{I}$.

The left and right state variables $\boldsymbol{q}_L$ and $\boldsymbol{q}_R$ at each $\{ij\}$ interface are needed to evaluate the fluxes. The flux for the unstructured scheme uses either linear (second-order) or quadratic (third-order) reconstruction to obtain values of $\boldsymbol{q}_L$ (or $\boldsymbol{q}_R$) from nodal values $\boldsymbol{q}_i$, $\boldsymbol{q}_j$, and the gradient $\nabla\boldsymbol{q}$ at point i (or j). For example, $\boldsymbol{q}_L$ is evaluated by

$$(\boldsymbol{q}_L)_i = \boldsymbol{q}_i + \phi[(1 - \psi)\nabla\boldsymbol{q}_i \cdot \vec{r}_{ij} + \psi^2(\boldsymbol{q}_j - \boldsymbol{q}_i)] \tag{25}$$

Here $\vec{r}_{ij}$ is the position vector from point i to the $\{ij\}$ control volume interface (the quadrature point), $\psi = 0$ for linear reconstruction, $\psi = 1/2$for quadratic reconstruction, and ϕ is a slope limiter. The Barth–Jesperson [18] limiter is used in this work to evaluate ϕ.

The gradient $\nabla\boldsymbol{q}_i$ in Eq. (25) is evaluated from an unweighted linear least-squares fit to solution values at point i and its neighboring points $j \in \mathscr{N}(i)$. This technique is discussed in detail by Anderson and Bonhaus [19] and Hyams [14], who also give formulas for the least-squares coefficients obtained by QR factorization. Values of $\boldsymbol{q}_R$ for this $\{ij\}$ cell interface are obtained by applying this same technique in the adjacent control volume centered at point j.

Viscous terms $\boldsymbol{G}$ are evaluated using a grid-transparent, directional derivative based method, wherein the velocity and temperature derivatives required for the evaluation of the shear stresses and heat flux are computed as

$$\nabla \boldsymbol{W}_{ij} \approx \frac{1}{2}(\nabla \boldsymbol{W}_i + \nabla \boldsymbol{W}_j) + \left[\boldsymbol{W}_j - \boldsymbol{W}_i - \frac{1}{2}(\nabla \boldsymbol{W}_i + \nabla \boldsymbol{W}_j)\cdot \vec{\Delta s}\right] \frac{\vec{\Delta s}}{|\vec{\Delta s}_{ij}|^2} \tag{26}$$

where $\boldsymbol{W} = [u\ v\ w\ T]$ and $\Delta s_{ij} = \vec{x}_j - \vec{x}_i$. The nodal gradients required in Eq. (26) are computed using a weighted least squares approach.

3.2. Time evolution

The nonlinear implicit scheme for both formulations can be written as

$$I_a \frac{\mathscr{V}_i}{\Delta t}\left[(1+\theta)\Delta \boldsymbol{Q}_i^n - \theta \Delta \boldsymbol{Q}_i^{n-1}\right] + \sum_{j\in\mathscr{N}(i)} \boldsymbol{H}_{ij}^{n+1}\delta\mathscr{S}_{ij} = (\mathbb{R}_{\boldsymbol{U}})_i^{n+1} = 0 \tag{27}$$

where $\theta = 0$ for a first order time discretization, and $\theta = 1/2$ for a second order time discretization. The matrix I_a is the identity matrix with the first entry zeroed for incompressible flows [20], and the full identity matrix for the arbitrary mach formulation; this ensures that the property $div(\vec{V}) = 0$ is preserved for incompressible flows for any time t.

The flow solver employs a discrete Newton relaxation approach based on that introduced by Whitfield and Taylor [21] and is given in the present context by

$$\frac{\mathscr{V}_i}{\Delta t}[(1+\theta)\boldsymbol{M}]_i^{n+1,m}\Delta_m \boldsymbol{q}_i^{n+1} \quad + \tag{28}$$

$$\sum_{j\in\mathscr{N}(i)} \delta\mathscr{S}_{ij}\left[\left(\frac{\partial \boldsymbol{H}_{ij}}{\partial \boldsymbol{q}_{L_{ij}}}\right)^{n+1,m}\Delta_m \boldsymbol{q}_i^{n+1} + \left(\frac{\partial \boldsymbol{H}_{ij}}{\partial \boldsymbol{q}_{R_{ij}}}\right)^{n+1,m}\Delta_m \boldsymbol{q}_j^{n+1}\right] = -(\mathbb{R}_{\boldsymbol{U}})_i^{n+1,m} \tag{29}$$

where

$$\Delta_m \boldsymbol{q}^{n+1} = (\boldsymbol{q}^{n+1,m+1} - \boldsymbol{q}^{n+1,m}) \tag{30}$$

Newton's method is used to drive the unsteady residual to zero. The partial derivatives $\partial \boldsymbol{H}/\partial \boldsymbol{q}$ arising from this linearization can be evaluated using numerical derivatives or the complex Taylor series method. They can also be replaced by approximations which result in substantial savings in computational time. The resulting linear system is solved using a Symmetric Gauss Seidel algorithm (point relaxation). For grids in motion, the Geometric Conservation Law (GCL) must be satisfied in order to prevent the occurrence of spurious sources in the solutions. This leads to an additional contribution to the residual $\mathbb{R}_{\boldsymbol{U}}$, and is discussed in detail in [14].

3.3. Turbulence modeling

The turbulence models are implemented in a loosely coupled manner. The flow solver has the Spalart–Allmaras model, the Menter SAS model, the $k-\epsilon/k-\omega$ hybrid model (with and without SST), and the Wilcox Reynolds Stress model. In addition, DES modes are available for the Spalart–Allmaras, the Menter SAS and the $k-\epsilon/k-\omega$ hybrid models [22]. No wall functions or transition models were used in either solver with integration being performed to the wall on grids designed to give y^+ values less than unity.

3.4. Parallel implementation

The parallel solution procedure consists of a scalable solution algorithm implemented to run efficiently on subdomains distributed across multiple processes and communicating via MPI. The algorithm has multiple nested kernels viz. time step, Newton iteration, LU/SGS iteration etc., and the subdomain coupling is at the innermost level, i.e., in the solution of the linear system. A block-Jacobi type updating of the subdomain boundaries ensures efficient parallelization with a small incremental cost incurred in terms of subiterations required to recover the convergence rate of the sequential algorithm. Details of the parallel algorithm can be found in Hyams [14].

4. Results

4.1. Model scale: GCM

The results presented here include the GCM at 0 and 10° yaw. These were two of the test cases chosen from the available experimental data. The simulation domain includes the NASA Ames $7' \times 10'$ tunnel as well as the GCM geometry. The reason for this was that the experimental pressure coefficient was referenced to a specific location on the test section wall, and including the tunnel allows a straightforward comparison between computed and experimental pressure distributions. A three-view of the GCM geometry is shown in Fig. 1. The relative locations of the various pressure taps on the GCM tractor and trailer are shown in Figs. 2 and 3, respectively.

The grids for both 0 and 10° yaw cases were generated using a combination of Gridgen (for the tetrahedral portion) and HUGG [23] (for inserting the viscous layers), and both consisted of the full geometry embedded in the wind tunnel. No symmetry plane assumption was used even on the 0° yaw case, given that flow unsteadiness around the tractor–trailer configuration is expected to destroy any inherent flow symmetry. The 0° yaw case consisted of approximately 20.5M points, and 66M elements (primarily tetrahedra and prisms); the 10° yaw case consisted of approximately

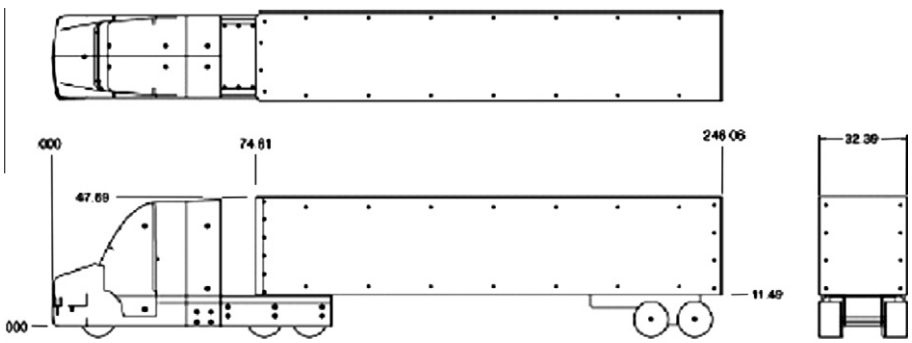

Fig. 1. Three-view drawing of the GCM tractor–trailer configuration (measurements in cm) [5].

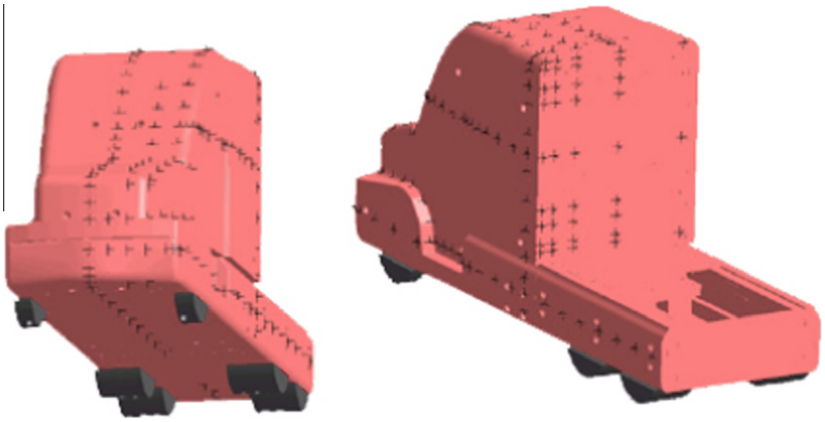

Fig. 2. Relative pressure tap locations on the GCM tractor [5].

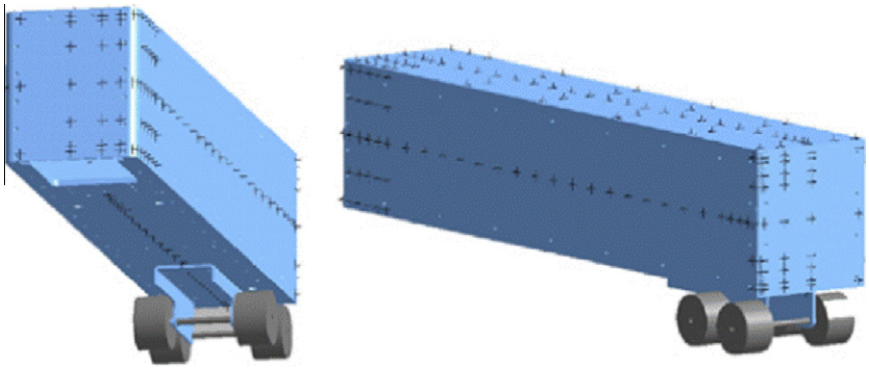

Fig. 3. Relative pressure tap locations on the GCM trailer [5].

18.9M points and 65M elements. All the cases presented here were run on 200 processors at a Reynolds number of 1.15×10^6 and a tunnel test section Mach number of 0.15. The average y^+ for all viscous surfaces was less than unity. Furthermore, all physical dimensions are scaled by the GCM model trailer width ($w = 12.75$ in.).

All of the present results were computed on the UT SimCenter's Dell 1300-core 325-node diskless Linux cluster, which is configured with dual-core Intel EM64T 3.0 GHz Xeon processors, 4 GB RAM per node, and a nonblocking gigabit interconnect consisting of a 576-port Force 10 E1200 switch.

4.1.1. Zero degree yaw

The solution for this case was obtained using the one equation Menter-SAS turbulence model that was operated in the DES mode. Since this simulation was started from uniform flow conditions, a spatially varying time step with a local CFL of 25.0 was used during an initial transient startup period of 5000 time steps. After the initial solution had reached a quasi-steady state, the solver was switched to an unsteady mode and the run was continued for a further 47,500 time steps. In the unsteady mode, a nondimensional time step of 10^{-3} was used together with three Newton subiterations to ensure time accuracy. Second order accuracy in time and a quadratic reconstruction in space were used to ensure higher order accuracy in time and space. To orient the reader, Fig. 4 shows the surface geometry of the GCM shaded by pressure coefficient.

Fig. 5 shows the unsteady axial force history as a function of time step. Although the axial force initially appears to diverge, it eventually attains an almost periodic state. Indeed, a time average of the axial force coefficient over the last 10,000 time steps yields an average value of 0.4203 as opposed to an experimental value of 0.4060. The computed fluctuations in axial force are about 10% of the average value.

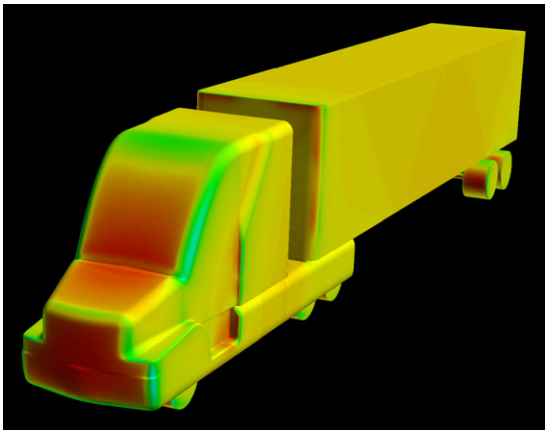

Fig. 4. GCM surface geometry shaded by pressure coefficient.

The sources of the unsteadiness are illustrated by Fig. 6, which shows axial velocity contours on a cutting plane at approximately the trailer half-height. The primary sources are the gap between the trailer and the tractor (tractor base region) and the base region of the trailer. Furthermore, the GCM model is mounted on cylindrical posts which, when placed in a crossflow, create unsteadiness in the flow field. As can be seen from the figure, there is a distinct pattern of vortex shedding originating from the tractor–trailer gap, and the base flow of the trailer is asymmetric as well. The asymme-

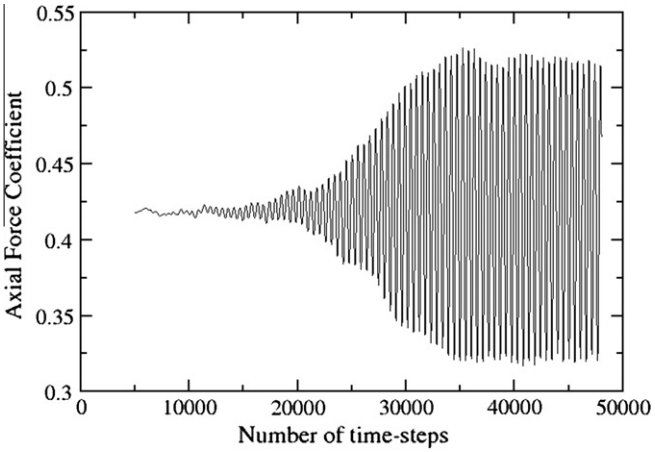

Fig. 5. Unsteady axial force coefficient history.

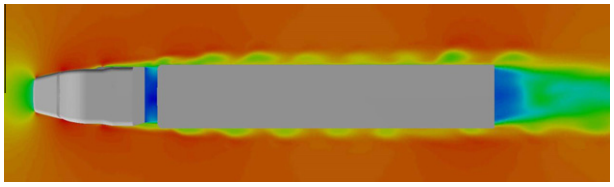

Fig. 6. Instantaneous axial velocity contours.

try on the shed vortex pattern between the two sides of the trailer as well as the asymmetry of the base flow clearly indicates that imposing an arbitrary symmetry condition on the flow field would not be correct; and for this reason, the entire domain was simulated.

To filter out the effects of the unsteadiness, the solution was time averaged over 1000 time steps. This frequency was picked arbitrarily; however, it does match the frequency in the axial force history fairly closely. In the next set of figures, time averaged and steady pressure coefficients are compared to experimental data. Figs. 7 and 8 show a comparison of pressure distribution along the centerline of the tractor. The two different views are for the centerline, with the difference being that one is plotted against the vertical coordinate (Fig. 7), while the other is plotted against the horizontal coordinate (Fig. 8). As can be seen from the two figures, the agreement between the experimental data and computations is very good. The effect of unsteadiness is not very significant along the centerline of the tractor.

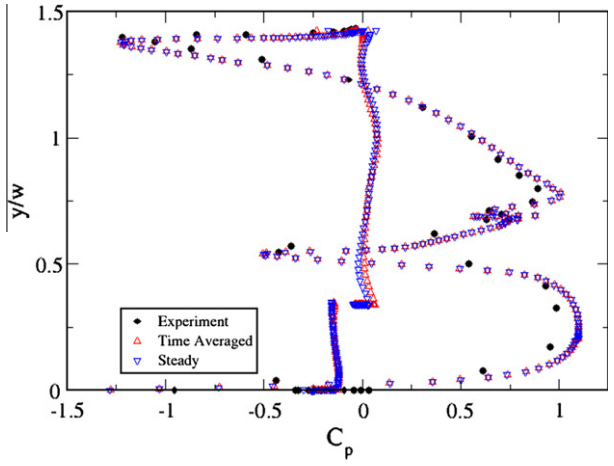

Fig. 7. Comparison of tractor centerline pressure distribution for 0° yaw, plotted against the vertical coordinate.

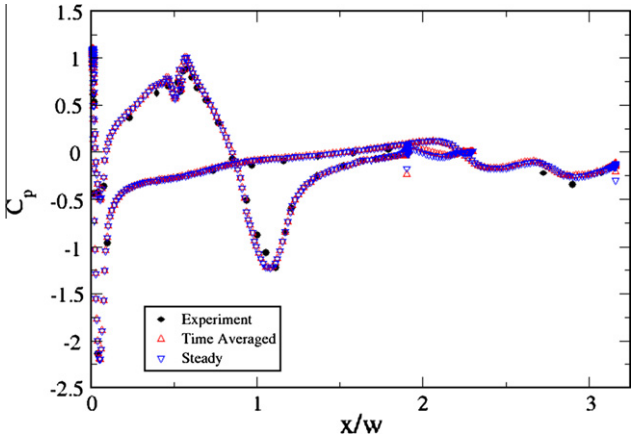

Fig. 8. Comparison of tractor centerline pressure distribution for 0° yaw, plotted against the horizontal coordinate.

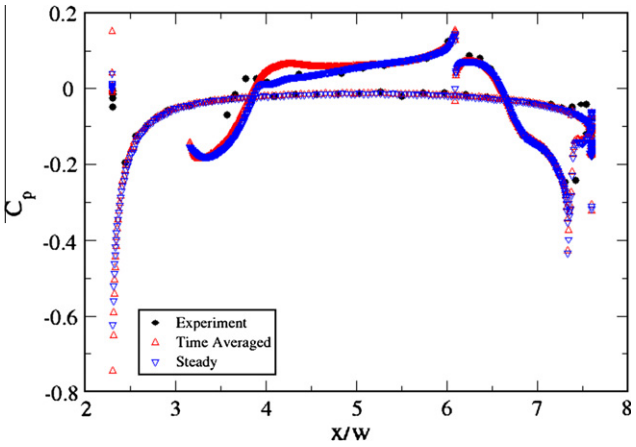

Fig. 9. Comparison of trailer centerline pressure distributions for 0° yaw.

Figs. 9 and 10 shows a comparison of pressure distributions for the trailer. Fig. 9 is a comparison along the centerline of the trailer. As can be from the figure, the effect of unsteadiness is not significant (especially over the top of the trailer), although it has an effect on the bottom side of the trailer. This is likely being caused by the presence of the cylindrical posts that were used to mount the model to the floor of the wind tunnel. Fig. 10 shows a comparison for the side of the trailer at approximately the trailer half-height. Again, the pressure distribution is not affected substantially by the time averaging. As can be seen from the figure, the comparisons between the experimental and computed results are excellent.

Comparisons of base pressures for the tractor as well as the trailer are shown in Figs. 11 and 12, respectively. The effect of unsteadiness is more visible here; however, one has to take account of the scale of the pressure distributions. In the previous figures, they had a typical range of 1.0 or higher. In this case, the range of the pressure coefficient is only 0.2, thereby potentially exaggerating some of the visual effect. In spite of this scale effect, the time averaged values track the experimental pressure distributions reasonably well.

4.1.2. Ten degree yaw

The solution for this case was obtained using the two-equation $k-\epsilon/k-\omega$ running for 20,000 time steps using a fixed local CFL of 25.0 in a non-DES mode. Then, the DES turbulence model that was

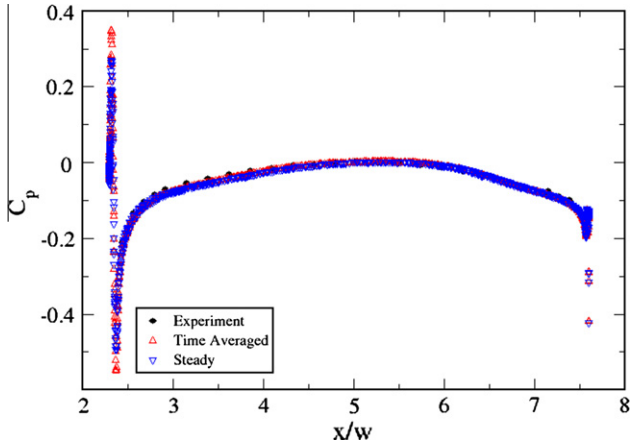

Fig. 10. Comparison of trailer side pressure distributions for 0° yaw, at trailer half-height.

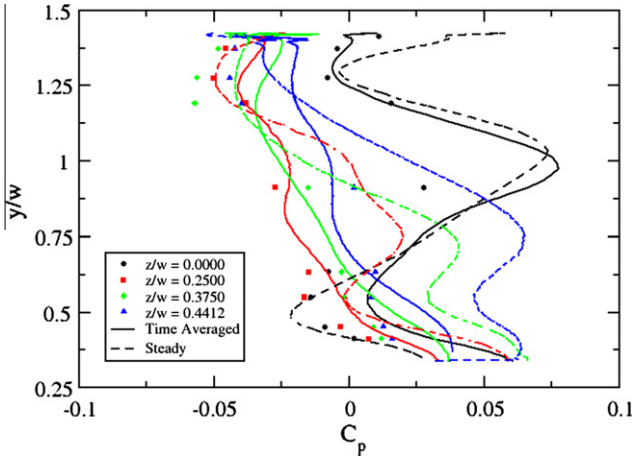

Fig. 11. Comparison of base pressure distributions on the tractor for 0° yaw.

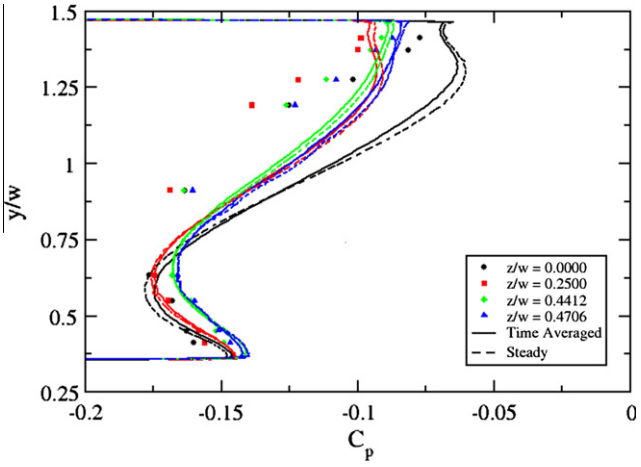

Fig. 12. Comparison of base pressure distributions on the trailer for 0° yaw.

operated in the DES mode. An initial solution was obtained by mode was activated and the solution continued for a further 10,000 time steps. The solver was then switched to an unsteady mode, and the run was continued for a further 30,000 time steps. In the unsteady mode, a nondimensional time step of 5×10^{-4} was used together with three Newton subiterations to ensure time

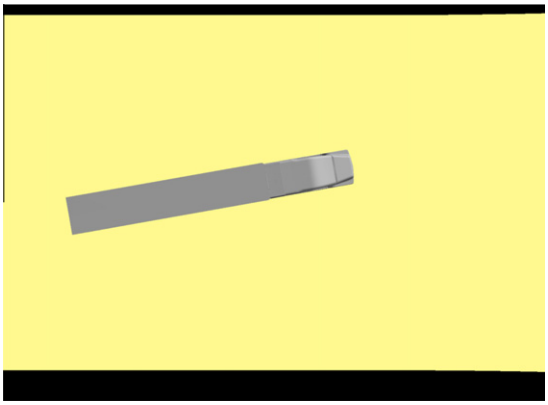

Fig. 13. Aerial view of the GCM model in the $7' \times 10'$ tunnel at 10° yaw (tunnel in yellow). (For interpretation of the references to colour in this figure legend, the reader is referred to the web version of this article.)

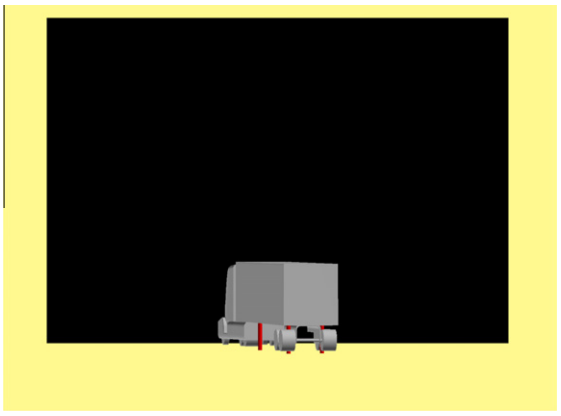

Fig. 14. Rear view of the GCM model in the $7' \times 10'$ tunnel at 10° yaw (tunnel in yellow). (For interpretation of the references to colour in this figure legend, the reader is referred to the web version of this article.)

accuracy. Second order accuracy in time and a quadratic reconstruction in space were used to ensure higher order accuracy in time and space. A geometric overview of the GCM inside the tunnel is shown in Figs. 13 and 14. Contours of instantaneous (at time step 57,500; 27,500 time step unsteady) helicity ($\vec{V} \times \vec{\omega}$, where $\vec{\omega}$ is the vorticity vector) and vorticity magnitude at approximately trailer half-height are shown in Figs. 15 and 16. As can be seen from the figures, a significant level of unsteadiness exists in the flowfield.

Unlike the 0° yaw case, the force history at the end of 30,000 unsteady time steps did not indicate any kind of periodic behavior. For the results presented here, the solutions were averaged over 1000 and 5000 time steps, which were arbitrary choices. Furthermore, the experiments were run so that yaw sweeps were conducted. This resulted in data being obtained for +10° as well as −10° yaw. Both of these experimental data are shown in the comparisons. This serves two purposes: (1) to highlight the level of the side-to-side uncertainty in the experimental measurements, and (2) to show the trailer was not instrumented on both the windward and leeward sides to the same extent. Therefore, using data from the positive and negative angles of yaw "fills in" the gap between the measurements.

Figs. 17 and 18 show a comparison of pressure distribution along the centerline of the tractor. Both sets of experimental data are shown along with the time averaged computed solutions. As can be seen from the figures, the agreement is very good between the experimental data and computations. The effect of the choice

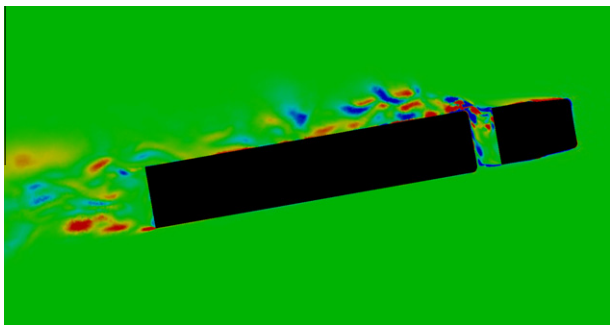

Fig. 15. Instantaneous helicity magnitude contours at $y/w = 0.9137$.

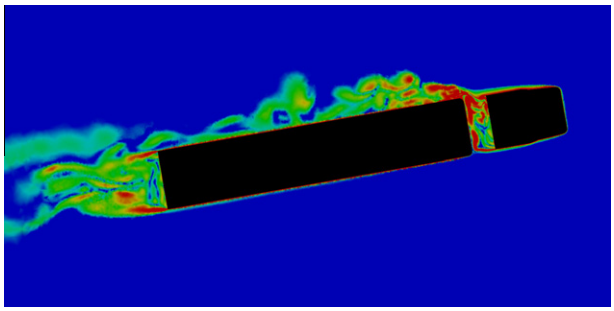

Fig. 16. Instantaneous vorticity magnitude contours at $y/w = 0.9137$.

in averaging period can be seen in both the plots. The 5000 time-step averaged solution appears to match the experimental data slightly better than the 1000 time-step averaged solution. Fig. 17 also demonstrates a significant discrepancy between the two experimental data sets taken for ±10° yaw in the region of $1.5 < x/w < 2.0$ (close to the base of the tractor). The computations match the +10° yaw results very closely in this area. Overall, the computations lie between the experimental data over the bulk of the centerline of the tractor.

A comparison of the trailer centerline pressure distribution on the top and bottom of the trailer is shown in Figs. 19 and 20, respectively. The data is presented in two different graphs for clarity. The computational results are repeated between Figs. 19 and 20, while only the top of the trailer data is shown in Fig. 19 and only the bottom of the trailer is shown in Fig. 20. As can be seen from Fig. 19, the trend towards the base of the trailer is not captured correctly by the computed results. There is also no significant

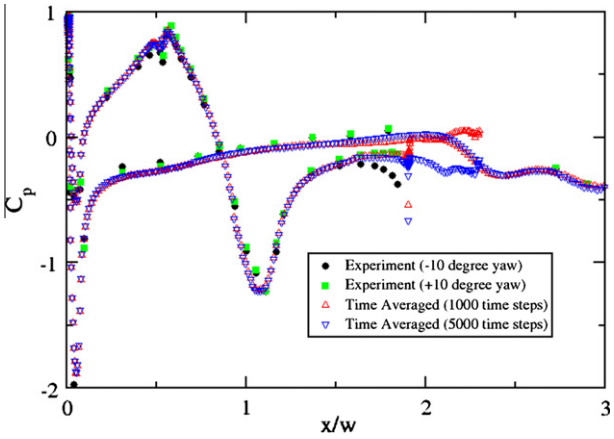

Fig. 17. Comparison of tractor centerline pressure distribution for 10° yaw, plotted against the horizontal coordinate.

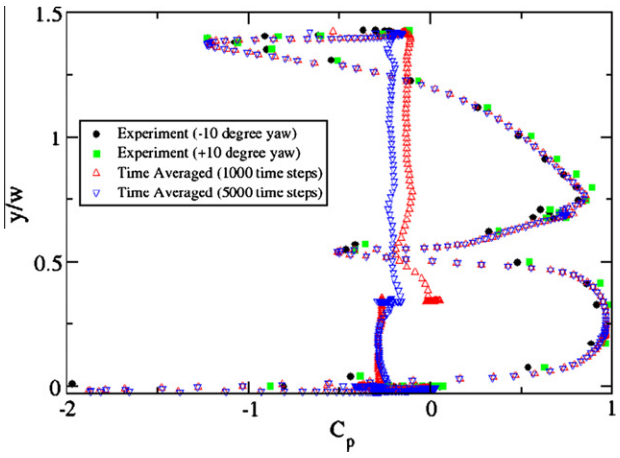

Fig. 18. Comparison of tractor centerline pressure distribution for 10° yaw, plotted against the vertical coordinate.

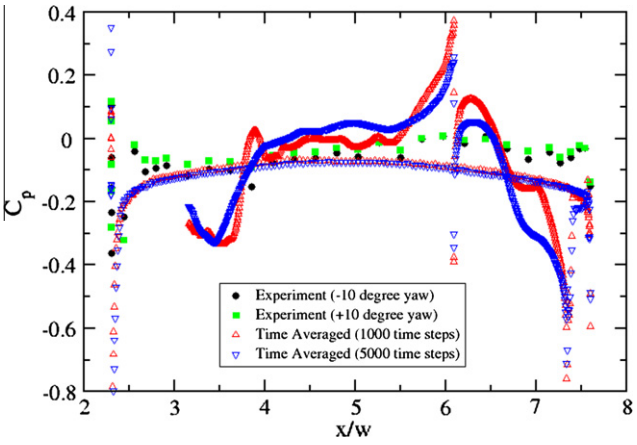

Fig. 19. Comparison of trailer centerline pressure distribution on the top of the trailer for 10° yaw.

difference between the 1000 and 5000 time-step averaged solutions. It is possible that the base flow region has a very strong influence on the pressure distribution in the neighborhood of the trailer base (some evidence of this can be seen in the 0° yaw case as well (Fig. 9). The comparison for the bottom of the trailer fares much

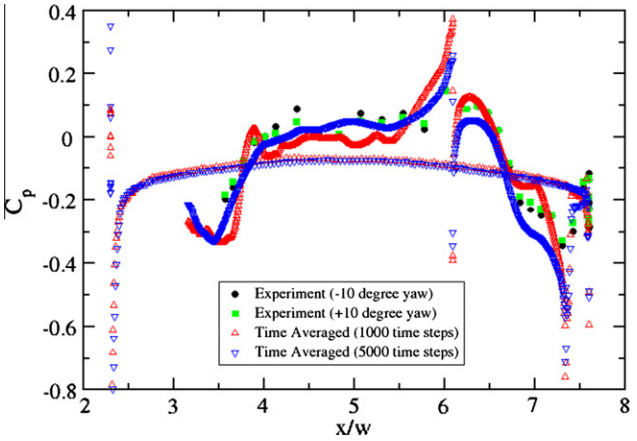

Fig. 20. Comparison of trailer centerline pressure distribution on the bottom of the trailer for 10° yaw.

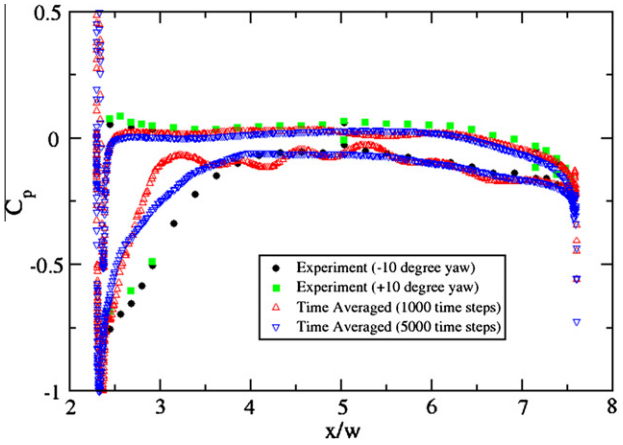

Fig. 21. Comparison of trailer pressure distribution at $y/w = 0.9137$ for 10° yaw.

better with the trend as well as the magnitude of the pressures being captured reasonably well (especially the 5000 time-step averaged solution).

The next comparison shown is for a line that is halfway up the side of the trailer (Fig. 21). As can be seen from the figure, the experimental data from the ±10° yaw provides a better picture of the overall pressure distribution on the trailer. The computations are reasonably close to the experimental data over the bulk of the trailer. The 5000 time-step averaged solution has smoothed out much of the fluctuation that is visible in the 1000 time-step averaged solution. The biggest discrepancy between the computed results and experimental data is at the front corner of the trailer. The experimental data seems to indicate a larger low pressure region (possibly caused by a large-scale vortex), while the computations indicate a much smaller low pressure region. Again, the 5000 time-step averaged solution compares much better to the experimental data than the 1000 time-step averaged solution. One of the reasons for this discrepancy could be that the grid resolution is inadequate in this area. Indeed, the surface grids for the 0 and 10° yaw cases were the same. In the ten degree case, there is significant flow through the tractor–trailer gap, while that was not the case for the 0° case; it could be necessary to resolve the flow features (both in terms of surface and volumetric resolution) in order to capture the flow physics correctly.

In addition to the lack of sufficient grid resolution, it is also possible that a more advanced turbulence model or perhaps an LES approach could provide a better resolution of flow features. Furthermore, the time averaging period was chosen arbitrarily and has a demonstrable, although limited, impact on the comparisons. A comparison of the axial and side forces is shown in Table 1. The numbers reported for the computed results are time averaged over the unsteady part of the run. As can be seen, there is a significant amount of variation between the two sets of experimental data, with the computation being within 10% of the experimental data for both positive and negative ten degree yaw.

4.2. Validation of rotating wheel

After the GCM model-scale simulations, the next natural step is to simulate full scale trucks under realistic conditions; i.e., with moving wheels and a moving ground plane. The isolated wheel experiment of Mears et al. [24] was used as a test case for validating the rotating wheel and moving ground plane boundary conditions. The geometry, shown in Fig. 22, consists of an isolated smooth wheel of radius 0.246 m in rotational contact with a moving ground plane moving at 14.7 m/s and in an air–stream moving at the same speed. The pressure coefficients along the wheel centerline computed using a steady simulation show excellent agreement when compared to time averaged experimental data in Fig. 23.

Table 1
Comparision of forces for the 10° yaw case.

Case	Axial force coefficient	Side force coefficient
Experiment (+10° yaw)	0.70980	+1.19873
Experiment (−10° yaw)	0.73849	−1.22730
Computed	0.80906	+1.31911

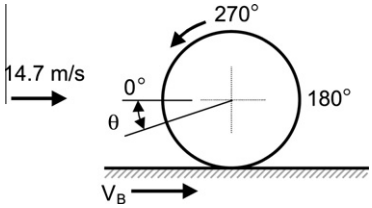

Fig. 22. Schematic of isolated wheel experiment and simulation.

During this validation, it was found that the pressure at the forward point of contact increases without bound under grid refinement. It is theorized that the wheel acts as a journal bearing and the actual pressure at the contact point is a function of the wheel weight and support mechanisms. A jet of air directed into the incoming flow was generated near the forward contact patch as a result of the convergence of two viscous moving boundaries, as seen in the velocity vectors in Fig. 24. This jet had a velocity magnitude of approximately half the freestream velocity as predicted by Fackrell [25].

A wheel-in-wheelhouse-cavity experiment by Axon et al. [26] was used to further validate the wheel and ground boundary conditions in the presence of more realistic support structures. The geometry, shown in Fig. 25, was recreated from the limited amount of information available in the paper. The wheel had a diameter of 0.5 m and the free-stream flow velocity was 25 m/s. Computed pressures along the two vertical and one horizontal inside surfaces of the wheelhouse are compared to experiment in Figs. 26–28. Especially given the large uncertainty in the specification of the geometry, the agreement with experimental data is very good.

4.3. Full scale simulations

A modified version of the GCM geometry (Fig. 29) scaled for full scale Reynolds numbers, was chosen as the base geometry for the

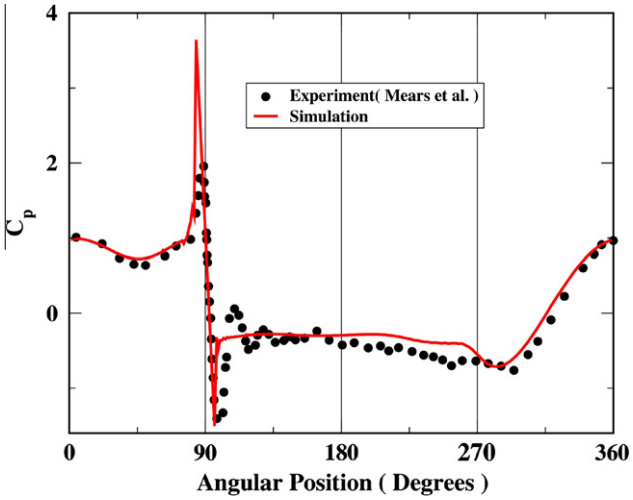

Fig. 23. Centerline pressure coefficients for isolated wheel.

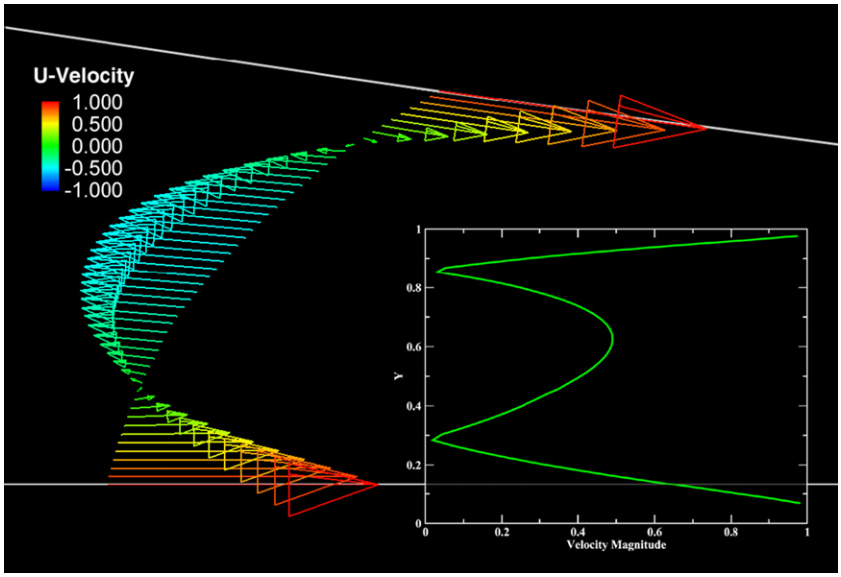

Fig. 24. Jetting near forward contact patch with velocity magnitude plot.

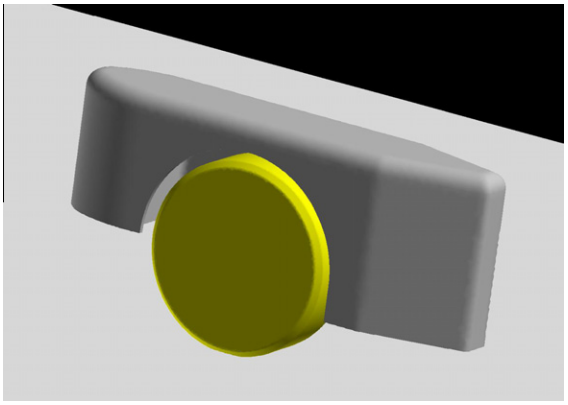

Fig. 25. Wheel-in-wheelhouse geometry.

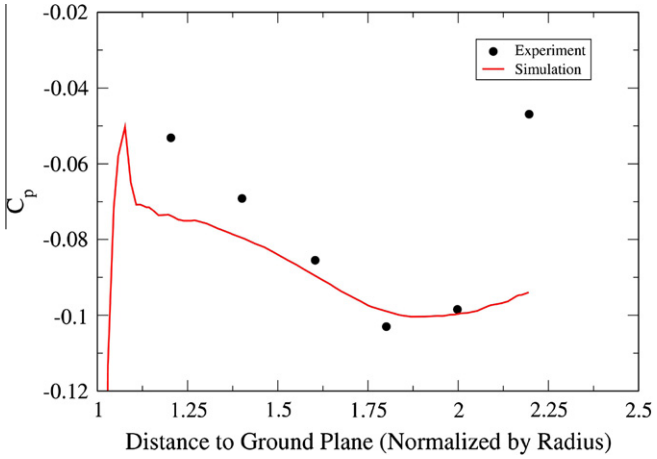

Fig. 26. Pressure comparisons along the front of the cavity.

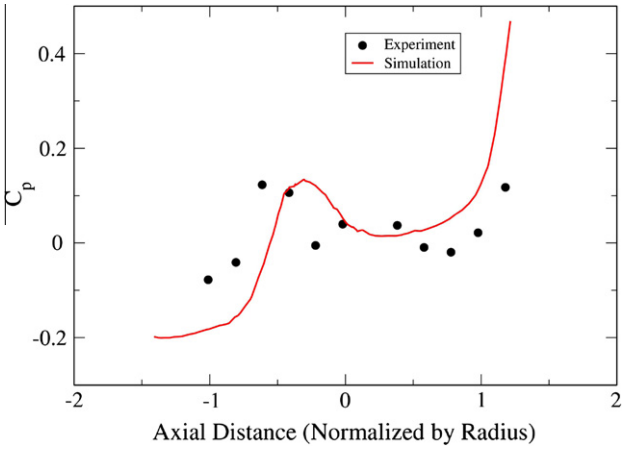

Fig. 27. Pressure comparisons along the top of the cavity.

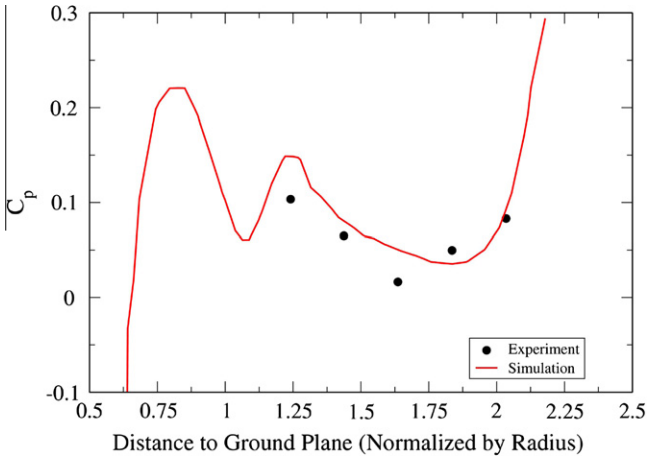

Fig. 28. Pressure comparisons along the back of the cavity.

simulations in this section of the study. The modifications include the addition of cab extenders and lowering of the geometry to allow the wheels to make contact with the ground plane. The support struts used for mounting the geometry in the wind-tunnel were also removed. Fillets were introduced at the contact line between the wheel and the ground plane in order to facilitate the grid generation process.

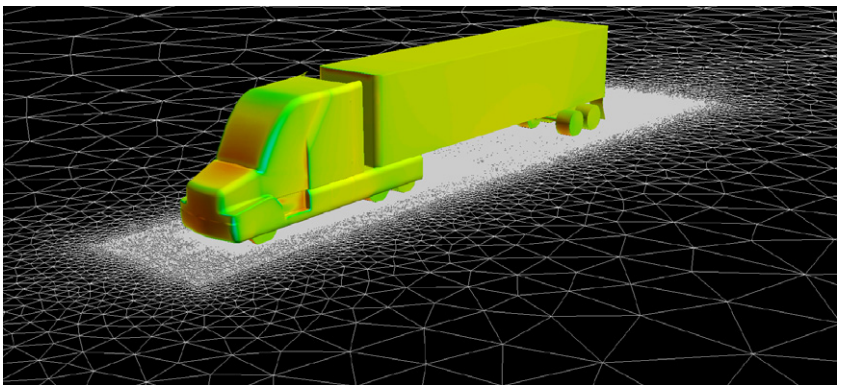

Fig. 29. Full scale truck geometry and ground plane mesh.

Like the model scale cases, a combination of GridGen and HUGG [23] was used to generate the grid for the full scale simulations. The off-wall spacings and growth parameters used were based on $y^+ \sim 1$ constraints and experience gained in the course of the validation process. The grids used here have approximately 1.1M surface elements on the truck surface and 18M control volumes in the field. Total time to solution for each case was 3 days on 200 processor cores using the same hardware as was utilized for the model-scale geometry.

Full scale Reynolds number was computed to be 5.15M based on a trailer width of 8.5 feet and a road speed of 65 mph. All simulations used a moving ground plane matching the road speed and rotating rear wheels on the trailer. Rotating wheels were incorporated into the simulation via a slip boundary condition described in the previous section.

Wind-averaged drag simulations were conducted assuming a 7 mph crosswind at six (15°, 45°, 75°, 105°, 135° and 165°) orientations with respect to the direction of travel of the truck. The wind-averaging procedure follows the method of Ingram [27] as described in Ortega [12], except that the drag forces are compared in the form of nondimensional force coefficients calculated using the road speed as reference.

For computational economy, the incompressible flow formulation in Tenasi was used for the following calculations. Because the wind speed is smaller in the full scale case than in model scale, it is expected that Mach numbers will be correspondingly smaller; therefore, compressibility is expected to play a very minor role in the overall solution.

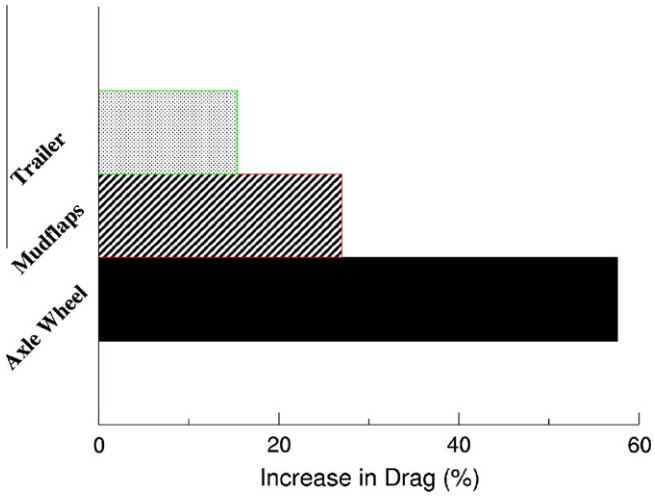

Fig. 30. Contributors to the drag increase caused by nonspinning wheels.

4.3.1. Effect of spinning wheels

In order to evaluate the effect of spinning wheels on the drag of the truck, the 45° crosswind case with mud flaps was run with the spinning wheel boundary condition deactivated. It was found that with stationary wheels, the drag increased by 5.4% over the spinning wheel case, with more than half the increment being due to an increase in the drag on the axle–wheel assembly as shown in Fig. 30. Increased drag on the mud flaps and trailer contributed to 27% and 15% of the total, respectively.

4.3.2. Cab extenders and splitter plates

The baseline truck geometry, which does not have cab extenders, exhibits large drag increases in the presence of crosswinds. This effect can be almost totally mitigated by the addition of cab extenders or splitter plates on the front face of the trailer. Neither of these devices has any effect in the absence of crosswinds. Adding both devices provides no additional drag benefit. Since trailers are much more prevalent than tractors, cab extenders are likely the more economical option, and they seem to have been universally adopted. The full scale GCM with cab extenders was chosen as the base model against which all drag reduction devices would be compared.

4.3.3. Base flaps

The base flaps consist of four panels inclined at an angle of 15° to the axis of the truck as shown in Fig. 31. Each panel is one-quarter of the width of the trailer (approximately 2.1 feet). This device has been extensively studied by other researchers, and a commercial product is available as well. This case was examined to ensure that the drag reduction from this study was in qualitative agreement with the results in the literature. The computed wind-averaged drag reduction of 15% compares favorably with tunnel scale model tests (~14%) [28], track tests (~8.4%) [29] and road tests

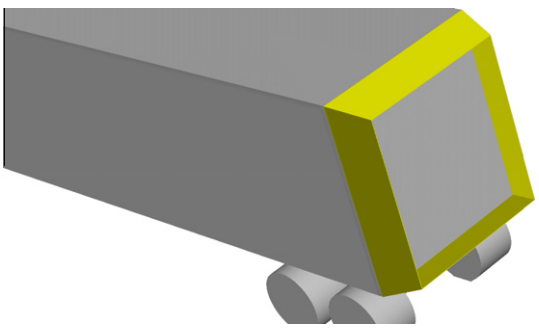

Fig. 31. Geometry of base flaps.

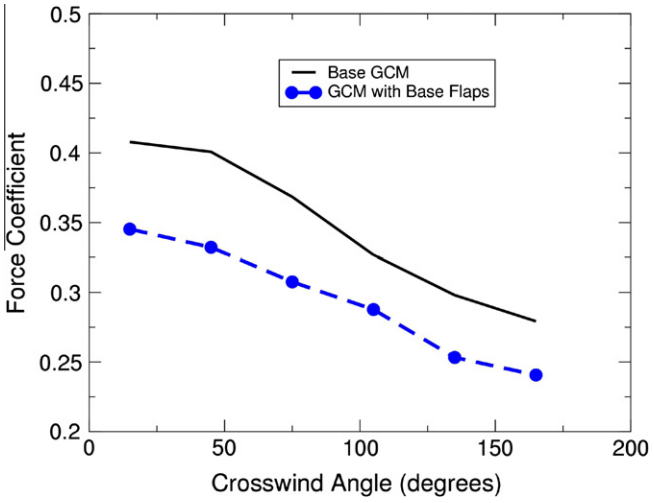

Fig. 32. Variation of axial force coefficient with crosswind angle.

(~12% and ~20%) [30] with full trucks. The wind tunnel data was for the GCM geometry and is therefore in close agreement. The track and road tests were for actual Class 8 trucks, and the drag numbers are derived from fuel savings assuming that the percentage fuel saving was half the drag reduction percentage.

The drag force coefficients at the various crosswind angles are shown in Fig. 32. The effectiveness of the base flap was not particularly sensitive to the direction of the crosswind, although it performs slightly better in head winds.

4.3.4. Front spoiler

Front spoilers have been used in cars for a few decades to reduce underbody drag and improve cooling airflow, but their effectiveness depends on careful sizing of the spoiler height [31]. The spoilers used in this study were approximately 3 in. in height and were located under the cab as shown in Fig. 33.

The front spoiler increased the wind-averaged drag on the truck by 0.2%. This implies that in an actual truck with front axles and other drag inducing components in the underbody region, the front spoiler could lead to small drag reductions. This is based on the fact that the drag increase due to the spoiler was 3.8%, while it reduced drag on the rest of the truck by 3.6%, even for a smooth underbody without front axles. Drag contributions from the truck components in the case are shown in Fig. 34. Lowered velocities in the underbody region account for the reduced drag on the tractor and wheel assembly as well as a portion of the reduced drag on the trailer. The majority of the trailer drag reduction comes from lowering of the pressure on the front face of the trailer due to changes in flow over and around the tractor. The drag values at the various crosswind angles shown in Fig. 35 are also encouraging, since the spoiler actually reduces drag when the truck is experiencing a head or tail-

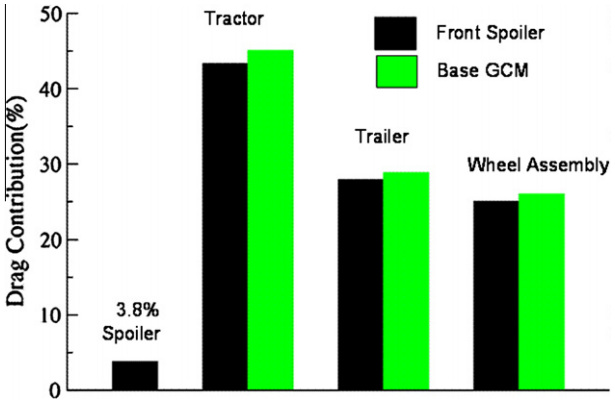

Fig. 34. Drag contributions of truck components.

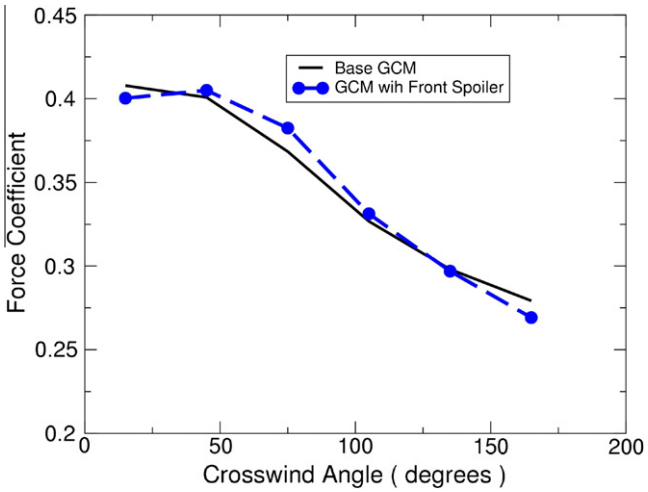

Fig. 35. Variation of axial force coefficient with crosswind angle.

wind. It might also be possible to modify the shape and/or height of the spoiler to reduce or eliminate the drag increase for non-parallel crosswinds. An accurate evaluation of this device will need simulations using a substantially more realistic truck model with underbody components and accurate capturing of the under-hood flow.

4.3.5. Mud flaps

Simulations were conducted to study the drag contribution of rear trailer mud flaps to the total drag and to look at ways in which this could be reduced. Full mud flaps which extend to the bottom of the trailer and half flaps that extend to the top the wheels as shown in Figs. 36 and 37, respectively, were studied. Full flaps

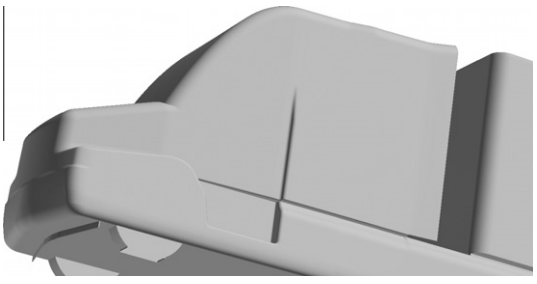

Fig. 33. Geometry and location of the front spoiler.

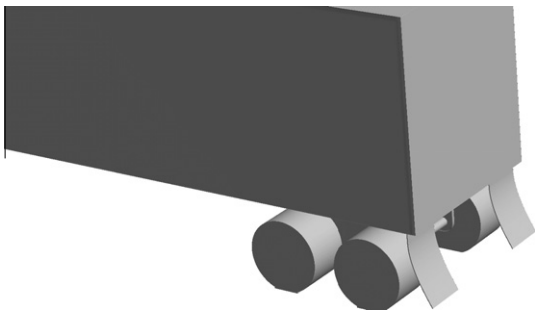

Fig. 36. Geometry of full mud flaps.

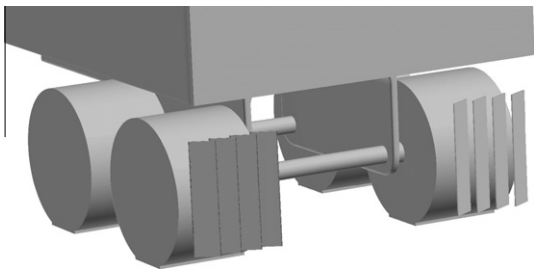

Fig. 37. Geometry of half slats.

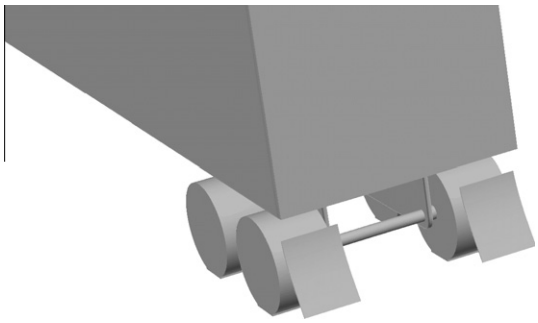

Fig. 38. Geometry of half mud flaps.

are usually used on trucks that transport shipping containers as well as on "pup" trailers. Half flaps are more common and are usually installed on most dry freight trailers.

The geometries of both flaps assume the presence of an anti-sail bracket with some curvature of the flaps beyond the device. A half slat (Fig. 38) was studied as a possible low drag alternative for half flaps. The slats are inclined at an angle of 45° to the flap plane and overlap each other to prevent straight flow through them. The wind-averaged drag value comparisons for the three components in Fig. 39 show that full flaps exact a heavy penalty by adding 8.6% to the drag, while the half flaps add only a modest 2.1%. The additional drag caused by half flaps can be completely eliminated by the use of half slats. Fig. 40 shows that the mud flap and trailer account for 78% and 74% of the total drag increase, while the wheel assembly experiences lower drag which accounts for 52% of the overall increase. The drag on the half-slats are almost identical to that on the baseline GCM for most crosswind angles as can be seen in Fig. 41.

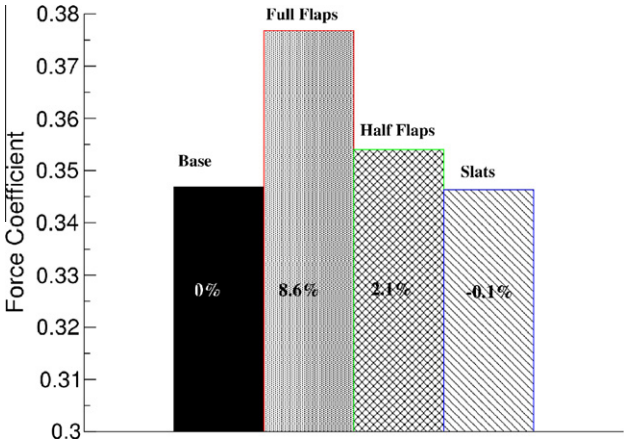

Fig. 39. Drag force coefficients of trucks with various mud flaps.

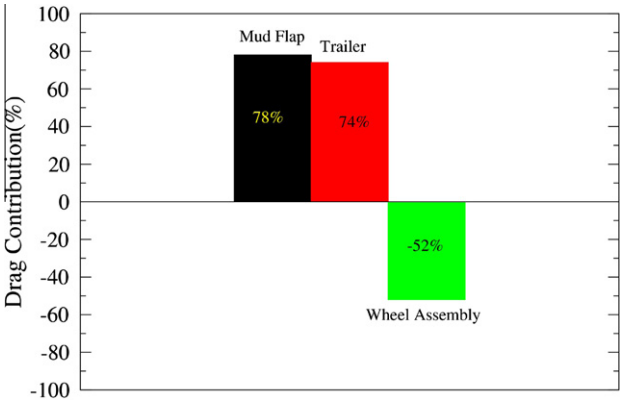

Fig. 40. Drag increase contributions for truck with full rear flaps.

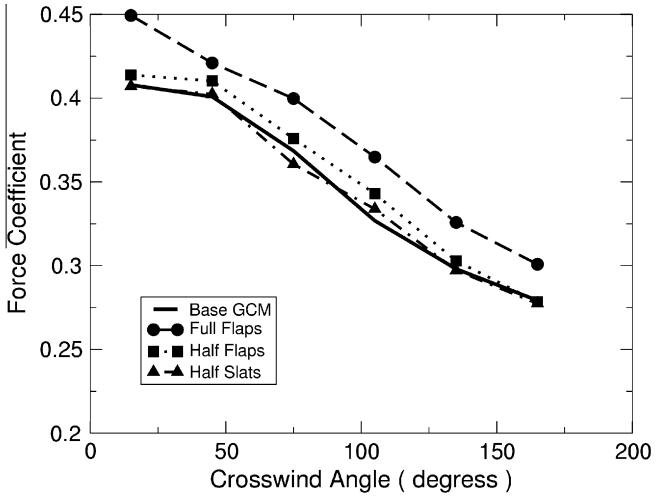

Fig. 41. Variation of drag with crosswind angle for truck with rear mud flaps.

5. Conclusion

Numerical solutions of the unsteady Reynolds-averaged Navier–Stokes equations using a parallel implicit flow solver have been given to investigate unsteady aerodynamic flows affecting the fuel economy of Class 8 trucks. The numerical algorithm used in the *Tenasi* family of field solvers is presented in both compressible and incompressible formulations. The finite volume discretization utilizes Riemann-based interfacial fluxes, and a fully nonlinear Newton iterative approach is used for the advancement of the solution variables in time. Shear stresses and heat fluxes are computed based on a directional derivative approach, and turbulence is modeled via DES versions of the one-equation Menter SAS and the two-equation $k-\epsilon/k-\omega$ model.

Computed forces and pressure coefficient distributions were compared to experimental data for the GCM tractor–trailer configuration for 0 and 10° yaw. Excellent agreement with experimental data was obtained for the 0° case while the 10° case had good agreement. The base pressures were predicted reasonably well for the 0° case. The 10 ° case pointed to the need for grid refinement in specific regions of the computational domain. It is also possible that the overall agreement for both the test cases could be improved by employing improved turbulence models.

The full scale simulations with and without spinning wheels indicate that a more realistic treatment of truck wheels is needed, particularly when evaluating components in close proximity to the wheels. The question of whether a simple smooth wheel with slip

boundary condition is an adequate model for the flow behavior near a real wheel with treaded tires and wheel holes cannot be answered without experimental studies and validation.

The base flap simulations demonstrate that the flow solver and grid resolution used in this study can produce a reasonable estimate of the relative magnitude of the drag reduction in the trailer base region despite the fact that validation studies show that CFD methods have a clear weakness in predicting flow features in this region. The implication is that a gross feature like the averaged pressure over the trailer back is being captured reasonably well while the smaller scale features are left unresolved. There is no guarantee that this will be true for any and all devices that work in the base area and therefore simulations should be looked upon with skepticism in the absence of supporting experimental evidence.

The front spoiler simulation did not predict any drag reduction for the full scale truck; however, the fact that the spoiler added only a negligible amount of drag indicates that the device is likely to reduce drag by a few percentage points for real truck with a significant amount of blockage in the underbody area.

A complete analysis of the mud flaps would require the solution of a coupled fluid-structures problem downstream of a fully detailed rotating wheel, and this problem was simplified considerably here in order to make it tractable. The results indicate that mud flaps, particularly full flaps, are extracting a rather high toll in terms of their drag contribution. The half slat simulations indicate that simple changes to the mud flaps might be sufficient to mitigate their drag contributions. Other components in that area such as the rear impact guard, the brake light panels and the license plate could possibly be redesigned to perhaps yield small drag savings as well.

Acknowledgements

This work was supported in part by the US Department of Energy and the Oak Ridge National Laboratory through UT-Batelle contract number 4000035270 with Dr. W. Keith Kahl as technical monitor. This support is gratefully acknowledged. Thanks are also due to Dr. Rose McCallen, Dr. Jules Routbort and the late Dr. Sid Diamond for their generous guidance and encouragement. This work was also supported by the THEC Center of Excellence in Applied Computational Science and Engineering with Dr. Harry McDonald as technical monitor. Their support is greatly appreciated.

References

[1] http://www.transportation.anl.gov/research/technology_analysis/truck_fuel_u.
[2] McCallen R, Couch R, Hsu J, Browand F, Hammache M, Leonard A, et al. Progress in reducing aerodynamics drag for higher efficiency of heavy duty trucks (Class 7–8). SAE Paper 1999-01-2238.
[3] Cooper KR. Truck aerodynamics reborn: lessons from the past. SAE Paper 2003-01-3376.
[4] Croll RH, Gutierrez WT, Hassan B, Suazo JE, Riggins AJ. Experimental investigation of the ground transportation systems (GTS) project for heavy vehicle drag reduction. SAE Paper 96-0907.
[5] Storms BL, Ross JC, Heineck JT, Walker SM, Driver DM, Zilliac GG. An experimental study of the ground transportation systems (GTS) project for heavy vehicle drag reduction. NASA Tech. Report TM-2001209621.
[6] Arcas D, Browand F, Hammache M. Flow structure in the gap between two bluff bodies. AIAA Paper 2004-2250.
[7] Storms B, Satran D, Heineck J, Walker S. A summary of the experimental results for a generic tractor–trailer in the Ames Research Center 7- by 10-foot and 12-foot wind tunnels. NASA TM-2006-213489.
[8] Salari K, Ortega J, Castellucci P. Computational prediction of aerodynamic forces for a simplified integrated tractor–trailer geometry. AIAA Paper 2004-2253.
[9] Pointer D. Evaluation of commercial CFD code capabilities for prediction of heavy vehicle drag coefficients. AIAA Paper 2004-2254.
[10] Maddox S, Squires K, Wurtzler KE, Forsythe J. Detached-eddy simulation of the ground transportation system. Aerodynam Heavy Vehicles: Trucks Buses Trains 2004:89–104.
[11] Roy C, Payne J, McWherter-Payne M, Salari K. RANS simulations of a simplified tractor/trailer geometry. Aerodynam Heavy Vehicles: Trucks Buses Trains 2004:207–18.
[12] Ortega J, Dunn T, McCallen R, Salari K. Computational simulation of heavy vehicle trailer wake. Aerodynam Heavy Vehicles: Trucks Buses Trains 2004:219–33.
[13] Sreenivas K, Hyams DG, Nichols DS, Mitchell B, Taylor LK, Briley WR, et al. Development of an unstructured parallel flow solver for arbitrary Mach numbers. AIAA Paper 2005-0325.
[14] Hyams DG. An investigation of parallel implicit solution algorithms for incompressible flows on unstructured topologies. Ph.D. thesis. Mississippi State University; May 2000.
[15] Hyams DG, Sreenivas K, Sheng C, Briley WR, Marcum DL, Whitfield DL. An investigation of parallel implicit solution algorithms for incompressible flows on multielement unstructured topologies. AIAA Paper 2000-0271 38th aerospace sciences meeting and exhibit, January 2000, Reno, NV.
[16] Briley WR, Taylor LK, Whitfield DL. High-resolution viscous flow simulations at arbitrary mach number. J Comput Phys 2003;184:79–105.
[17] Chorin AJ. A numerical method for solving incompressible viscous flow problems. J Comput Phys 1967;2:12–26.
[18] Barth T, Jesperson D. The design and application of upwind schemes on unstructured meshes. AIAA Paper 93-0192.
[19] Anderson WK, Bonhaus DL. An implicit upwind algorithm for computing turbulent flows on unstructured grids. Comput Fluids 1994;23(1):1–21.
[20] Taylor LK, Arabshahi A, Whitfield DL. Unsteady three-dimensional incompressible Navier–Stokes computations for a prolate spheroid undergoing time-dependent maneuvers. AIAA Paper 95-0313 33rd Aerospace sciences meeting and exhibit, January 1995, Reno, NV.
[21] Whitfield DL, Taylor LK. Discretized Newton-relaxation solution of high resolution flux-difference split schemes. AIAA Paper 91-1539.
[22] Nichols D, Hyams D, Sreenivas K, Mitchell B, Taylor L, Whitfield D. Aerosol propagation in an urban environment. AIAA Paper 2006-3726.
[23] Karman S. Unstructured viscous layer insertion using linear-elastic smoothing. AIAA Paper 2006-0531.
[24] Mears A, Crossland SC, Dominy R. An investigation into the flow field about an exposed racing wheel. Vehicle Aerodynamics 2004. SAE 2004–01–0446.
[25] Fackrell JE. The aerodynamics of an isolated wheel rotating in contact with the ground. Ph.D. thesis. University of London; 1974.
[26] Axon L, Garry K, Howell J. The influence of ground condition on the flow around a wheel located within a wheelhouse cavity. SAE Technical Paper 1999-01-0806.
[27] Ingram KC. The wind-averaged drag coefficient applied to heavy goods vehicles. Transport and road research laboratory supplementary report 392.
[28] Storms BL, Satran DR, Heineck JT, Walker ST. A study of Reynolds number effects and drag-reduction concepts on a generic tractor–trailer. AIAA Paper 2004-2251.
[29] Browand F, Radovich C, Boivin M. Fuel saving by means of flaps attached to the base of a trailer: field test results. SAE Paper 2005-01-1016.
[30] McCallen R et al. DOEs effort to reduce truck aerodynamic drag through joint experiments and computations. <www.eere.energy.gov/vehiclesandfuels/pdfs/hvso_2006/02_mccallen.pdf>.
[31] Hucho WH. Aerodynamics of road vehicles: from fluid mechanics to vehicle engineering. SAE international.